arXiv:astro-ph/0003310v1 22 Mar 2000

To appear in ApJ

Photometry and Photometric Redshifts of Faint Galaxies in the Hubble Deep Field South NICMOS Field[1,2]

Noriaki Yahata, Kenneth M. Lanzetta, Hsiao-Wen Chen,
Alberto Fernández-Soto, Sebastian M. Pascarelle, and Amos Yahil

Department of Physics and Astronomy, State University of New York at Stony Brook, Stony Brook, NY 11794–3800, U.S.A.

and

Richard C. Puetter

Center for Astrophysics and Space Sciences, University of California at San Diego, La Jolla, CA 92093–0424, U.S.A.

ABSTRACT

We present a catalog of photometry and photometric redshifts of 335 faint objects in the HDF–S NICMOS field. The analysis is based on (1) infrared images obtained with the Hubble Space Telescope (HST) using the Near Infrared Camera and Multi-Object Spectrograph (NICMOS) with the F110W, F160W, and F222M filters, (2) an optical image obtained with HST using the Space Telescope Imaging Spectrograph (STIS) with no filter, and (3) optical images obtained with the European Southern Observatory (ESO) Very Large Telescope (VLT) with U, B, V, R, and I filters. The primary utility of the catalog of photometric redshifts is as a survey of faint galaxies detected in the NICMOS F160W and F222M images. The sensitivity of the survey varies significantly with position, reaching a limiting depth of $AB(16,000) \approx 28.7$ and covering 1.01 arcmin^2 to $AB(16,000) = 27$ and 1.05 arcmin^2 to $AB(16,000) = 26.5$. The catalog of photometric redshifts identifies 21 galaxies (or 6% of the total) of redshift $z > 5$, 8 galaxies (or 2% of the total) of redshift $z > 10$, and 11 galaxies (or 3% of the total) of best-fit spectral type E/S0, of which 5 galaxies (or 1% of the total) are of redshift $z > 1$.

---

[1]Based on observations with the NASA/ESA Hubble Space Telescope, obtained at the Space Telescope Science Institute, which is operated by the Association of Universities for Research in Astronomy, Inc., under NASA contract NAS 5–26555.

[2]Based on observations collected at the European Southern Observatory, Paranal, Chile (VLT-UT1 Science Verification Program).

Subject headings: Cosmology: Observations — Galaxies: Distances and Redshifts — Galaxies: Photometry — Galaxies: Statistics

1. INTRODUCTION

The Hubble Deep Field South (HDF–S) images are among the deepest images of the universe ever obtained at optical and infrared wavelengths. In this paper, we present a catalog of photometry and photometric redshifts of 335 faint objects in the HDF–S NICMOS field. The analysis is based on (1) infrared images obtained with the Hubble Space Telescope (HST) using the Near Infrared Camera and Multi-Object Spectrograph (NICMOS) with the F110W, F160W, and F222M filters, (2) an optical image obtained with HST using the Space Telescope Imaging Spectrograph (STIS) with no filter, and (3) optical images obtained with the European Southern Observatory (ESO) Very Large Telescope (VLT) with U, B, V, R, and I filters. The analysis is similar to the analyses of the Hubble Deep Field (HDF) described previously by Lanzetta, Yahil, & Fernández-Soto (1996, hereafter LYF96) and Fernández-Soto, Lanzetta, & Yahil (1999, hereafter FLY99), although in detail the current analysis differs from the previous analyses in three important ways:

First, objects are detected in the NICMOS F160W and F222M images, at central wavelengths of $\lambda \approx 16,000$ Å and $\lambda \approx 22,200$ Å, respectively. The analysis is in principle sensitive to galaxies of redshift as large as $z \approx 18$, beyond which the Lyα-forest absorption discontinuity is redshifted past the response of the NICMOS F222M filter.

Second, the optical and infrared photometry is measured using a new quasi-optimal photometry technique that fits model spatial profiles of detected objects to the space- and ground-based images. The technique is based on but extends the spatial profile fitting technique described previously by FLY99. In comparison with conventional methods, the new technique provides higher signal-to-noise ratio measurements, and in contrast with conventional methods, the new technique accounts for uncertainty correlations between nearby, overlapping neighbors.

Third, the photometric redshifts are measured using our redshift likelihood technique with a sequence of six spectrophotometric templates, including the four templates of our previous analyses (of E/S0, Sbc, Scd, and Irr galaxies) and two new templates (of star-forming galaxies). Inclusion of the two new templates eliminates the tendency of our previous analyses to systematically underestimate the redshifts of galaxies of redshift $2 < z < 3$ (by a redshift offset of roughly 0.3), in agreement with results found previously by Benítez et al. (1998). Comparison with spectroscopic redshifts of galaxies identified in the HDF and HDF–S indicates that with the sequence of six spectrophotometric templates the photometric redshifts are accurate to within an RMS relative uncertainty of $\Delta z/(1+z) \lesssim 7\%$ at all redshifts $z < 6$ that have as yet been examined.

The primary utility of the catalog of photometric redshifts is as a survey of faint galaxies

detected in the NICMOS F160W and F222M images. The sensitivity of the survey varies significantly with position, reaching a limiting depth of $AB(16,000) \approx 28.7$ and covering 1.01 arcmin^2 to $AB(16,000) = 27$ and 1.05 arcmin^2 to $AB(16,000) = 26.5$. Likewise, the survey reaches a limiting depth of $AB(22,200) \approx 24.8$ and covering 0.79 arcmin^2 to $AB(22,200) = 24$ and 1.09 arcmin^2 to $AB(22,200) = 23$.

The organization of the paper is as follows: In § 2, the observations are described. In § 3, the object identification, photometry, and photometric redshift measurements are described. The results are presented in § 4, and the discussion is presented in § 5 and § 6. The summary and conclusions are given in § 7. Scientific analysis of the catalog will be presented in forthcoming papers.

2. OBSERVATIONS

The HDF–S NICMOS field is centered at J2000 coordinates α = 22:32:51.75 and $\delta = -60$:38:-48.20. The observations consist of three sets of images: (1) infrared images obtained with HST using NICMOS, (2) an optical image obtained with HST using STIS, and (3) optical images obtained with the ESO VLT using the Test Camera. Table 1 summarizes details of the observations.

The HST NICMOS images were acquired in September, 1998 using NICMOS with Camera 3 and the F110W, F160W, and F222M filters. For each band, the observations consisted of ≈ 100 dithered exposures of between 512 s and 1472 s duration. The raw images were processed and reduced by the Space Telescope Science Institute (STScI) NICMOS team. The processed images were registered onto a grid of 1100×1300 pixel^2 at a scale of 0.075 arcsec pixel^{-1}, which covers an angular area of $\approx 1 \times 1$ arcmin^2. The HST STIS image was acquired in September and October 1998 using STIS with the 50CCD in open filter mode (which is sensitive at wavelengths spanning $\lambda \approx 2000-10000$ Å). The observations consisted of 9 dithered exposures of 2900 s duration. The raw images were processed and reduced by the STScI STIS team. The processed image was registered onto a grid of 3300×3900 pixel^2 at a scale of 0.025 arcsec pixel^{-1}, which covers roughly the same angular area as the NICMOS images. We used the non-drizzled Version 1 release of the NICMOS and STIS images, which were made available by STScI on 23 November, 1998, and we adopted photometric zero points determined by the STScI NICMOS and STIS teams.

The ESO VLT images were acquired in August, 1998 using the Unit Telescope #1 (UT1) with the Test Camera and the U, B, V, R, and I filters as a part of the VLT science verification campaign (ESO VLT-UT1 Science Verification 1998). For each band, the observations consisted of ≈ 20 dithered exposures of ≈ 900 s duration. We reduced the raw images, taking extra care in constructing the flat-field images, because the Test Camera CCD suffers from a large, wavelength-dependent blemish in its center. In agreement with Fontana et al. (1999), we found that separate superflats constructed from the median of the images obtained each night work best. The processed images are sampled on a grid of $\approx 1000 \times 1000$ pixel^2 at a scale of 0.091 arcsec pixel^{-1}, which covers

an angular area of $\approx 1.5 \times 1.5$ arcmin^2. We adopted photometric zero points determined by Fontana et al. (1999).

The point spread functions (PSFs) of the ground-based images vary significantly from image to image, with the best images characterized by FWHM ≈ 0.5 arcsec and the worst images characterized by FWHM ≈ 2.2 arcsec. For this reason, we worked only with the individual images, i.e. without combining the images in each band.

We registered the ground-based images to the space-based images (because the space-based images were already registered to within ≈ 0.05 pixel by the STScI NICMOS and STIS teams). We registered the images by measuring coordinates of stars in the space- and ground-based images, using these measurements to derive transformations to the space-based frame, and shifting, rotating, and scaling the ground-based images to the space-based frame. Special treatment was required for the U-band images, for which only a single bright star is available. In this case, we shifted according to measurements of the star and rotated and scaled according to measurements from the other bands. Adjacent pixels of the final, registered images are correlated as a result of the reduction and registration procedures, which must be accounted for by the analysis.

3. ANALYSIS

3.1. Object Detection

We detected objects in the NICMOS F160W image following procedures similar to those described previously by LYF96 and FLY99. First, we formed a signal-to-noise image by dividing the F160W image by the square root of the F160W variance image. Next, we applied the SExtractor object detection program (Bertin & Arnouts 1996) to detect objects in the signal-to-noise image. We set the SExtractor detection parameters by requiring that no spurious objects were detected in the "negative" signal-to-noise image, which we formed by dividing the negative of the F160W image by the square root of the F160W variance image. We detected objects according to a signal-to-noise criterion (rather than a signal criterion) because the sensitivity of the F160W image varies significantly with position. (Generally, the image is more sensitive toward the center and less sensitive toward the edges as a consequence of the way the individual exposures were dithered.) Finally, we modified the resulting SExtractor segmentation map to make three small corrections: (1) we eliminated objects near the edges of the image, (2) we deblended objects around bright stars or galaxies, and (3) we merged diffraction spikes of bright stars to the host stars. A total of 332 objects were detected, the brightest of which is of magnitude $AB(16,000) \approx 17.2$ and the faintest of which is of magnitude $AB(16,000) \approx 29.2$.

We repeated the same detection procedures using the NICMOS F222M image. Three additional objects were detected and incorporated into the object catalog.

3.2. Photometry

We measured optical and infrared photometry using a new quasi-optimal photometry technique that fits model spatial profiles of the detected objects to the space- and ground-based images. The technique is based on but extends the spatial profile fitting technique described previously by FLY99. In particular, the current technique implements two improvements over the previous technique: First, we used an image reconstruction method to generate smooth models of the intrinsic spatial profiles of the objects, which allows the spatial profile fitting technique to be applied to the space-based images as well as the ground-based images. Second, we applied the spatial profile fitting technique to the individual ground-based images (without combining the images in each band), which is necessary in order to achieve optimal sensitivity given that the PSFs of the ground-based images vary significantly from image to image. In comparison with conventional methods, the new technique provides higher signal-to-noise ratio measurements, and in contrast with conventional methods, the new technique accounts for uncertainty correlations between nearby, overlapping neighbors.

First, we determined the PSFs of the space- and ground-based images. For the space-based images, we approximated the PSFs by the median average of the three faintest of the four brightest stars in each image. For the ground-based images, we approximated the PSFs by double Gaussian profiles

$$\Phi\left(r\right) = \sum_{i=1}^{2} A_i \exp\left[-\frac{1}{2}\left(\frac{r}{\sigma_i}\right)^2\right] \tag{1}$$

(where r is the distance from the profile center), where we estimated parameters by fitting to the brightest stars in each image (excluding saturated stars).

Next, we modeled the intrinsic spatial profiles of the objects. We produced the models by reconstructing the F160W and F222M images using the non-negative least-squares (NNLS) image reconstruction method (see Puetter & Yahil 1999, and references therein) and masking the reconstructed image with the SExtractor segmentation map to identify individual intrinsic spatial profiles of individual objects. Briefly, the NNLS image reconstruction method is an indirect image reconstruction method that constrains the reconstructed image to be non-negative, which forces the reconstructed image—i.e. the model image convolved with the PSF—to be smooth on the scale of the PSF. The NNLS image reconstruction method is matched to our purpose of modeling the intrinsic spatial profiles of the objects because it produces a smooth model of an image with the effects of the PSF removed.

Next, we formed image templates of the objects in the images by convolving the intrinsic spatial profiles of the objects with the appropriate PSFs of the images.

Finally, we fitted the image templates to the images to determine optimal flux estimates. For

the kth image of a given band, we calculated a χ^2 statistic of the form

$$\chi^2_k = \sum_{i,j} \left[\frac{I^{(k)}(i,j) - B^{(k)}(i,j) - \sum_{n=1}^{N} F_n P_n^{(k)}(i,j)}{\sigma_{\rm eff}^{(k)}(i,j)} \right]^2, \tag{2}$$

where $I^{(k)}$ is the image, $B^{(k)}$ is the background, $P_n^{(k)}$ is the image template, $\sigma_{\rm eff}^{(k)}$ is the effective uncertainty (described previously by FLY99) and F_n is the optimal flux estimate of the nth object and where the sum extends over all pixels in the image. We determined local backgrounds by median averaging within 64×64 pixel^2 boxes centered on the objects, excluding pixels occupied by any objects, and we determined effective uncertainties by summing the elements of 3×3 data covariance matrices. We formed the total χ^2 of a given band by summing the χ^2 statistic over all individual images, i.e.

$$\chi^2 = \sum_k \chi^2_k. \tag{3}$$

For the space-based images, only one image (i.e. the final processed image) enters into the sum, whereas for the ground-based images, ≈ 20 images (i.e. the individual exposures) enter into the sum. Given N objects detected in the image, we set $\partial\chi^2/\partial F_i = 0$ to yield a system of N coupled linear equations with N unknowns (i.e. the F_i, with $i = 1, N$). We solved the equations by Cholesky decomposition of the Hessian matrix to determine the optimal flux estimates F_i and the optimal flux uncertainty estimates σ_{F_i}. Note that the technique is applicable to a set of unadded images simply because the Hessian matrix of a given band is additive with respect to the individual images.

The signal-to-noise ratios obtained by the current method are in general substantially larger than the signal-to-noise ratios obtained by conventional methods, say by direct integration within isophotal apertures. This is demonstrated in Figure 7, which shows the signal-to-noise ratio obtained by the current method compared with the signal-to-noise ratio obtained by the aperture method versus object flux, for objects measured in the F160W, STIS, and VLT I-band images. For the majority of objects at all flux levels, the signal-to-noise ratio obtained by the current method is larger than the signal-to-noise ratio obtained by the aperture method, by a factor that is typically ≈ 2 but that ranges up to ≈ 10. The improvement is particularly substantial for the ground-based image where the PSFs vary significantly from exposure to exposure. For a small minority of objects, the signal-to-noise ratio obtained by the current method is formally smaller than the signal-to-noise ratio obtained by the aperture method. This is explained by noting that the current method accounts for uncertainty correlations between nearby, overlapping neighbors whereas the aperture method does not. In particular, by examining individual objects with low signal-to-noise ratio detections, we find that: (1) objects with overlapping neighbors of comparable flux levels have flux errors underestimated by aperture photometry due to significant contributions from the off-diagonal parts of the covariance matricies, and (2) objects with overlapping neighbors of much higher flux levels have flux measurements overestimated by aperture photometry because substantial amounts of flux from the brighter objects are incorrectly assigned to the fainter objects. These two errors of aperture photometry have the effect of falsely increasing the signal-to-noise

ratio of the aperture measurements at low signal-to-noise ratios. We therefore conclude that the current method is superior to conventional methods in two respects: (1) it provides substantially higher signal-to-noise ratios, and (2) it provides more realistic error estimates.

3.3. Photometric Redshifts

We measured photometric redshifts following procedures similar to those described previously by LYF96 and FLY99, but with a sequence of six spectrophotometric templates, including the four templates of our previous analyses (of E/S0, Sbc, Scd, and Irr galaxies) and two new templates (of star-forming galaxies).

First, we formed the two new spectrophotometric templates of star-forming galaxies by adopting ultraviolet- and optical-wavelength spectrophotometry of starburst galaxies of intrinsic color excess $E_{B-V} < 0.10$ (designated SB1) and $0.11 \leq E_{B-V} \leq 0.21$ (designated SB2) of Kinney et al. (1996) and extrapolating toward ultraviolet and infrared wavelengths and incorporating the effects of intrinsic and intervening absorption according to the prescription of FLY99. (Specifically, we assumed that galaxies are optically thick at the Lyman Limit and incorporated the average Lyman α and Lyman β decrement parameters of Madau 1995 and Webb 1996.) Figure 7 shows the spectrophotometric templates, which span rest-frame wavelengths $912 - 25,000$ Å.

Next, we integrated the spectrophotometric templates with the system throughput functions of each instrument with each filter. For the HST instruments, we adopted the system throughput functions provided by the STScI NICMOS and STIS teams. For the VLT instruments, we modeled the system throughput functions using filter and detector response functions provided by the VLT Science Verification team, instrument response functions calculated from the measured reflectivity of the Al reflecting surfaces, and a standard atmospheric response function. Figure 7 shows the system throughput functions.

Finally, we determined photometric redshifts by maximizing a likelihood estimator of the form

$$\mathcal{L}\left(z,T\right) = \prod_{i=1}^{9} \exp\left\{-\frac{1}{2}\left[\frac{f_i - AF_i\left(z,T\right)}{\sigma_i}\right]^2\right\}, \tag{4}$$

where f_i is the measured flux in band i, σ_i is the measured flux uncertainty in band i, $F_i(z,T)$ is the modeled flux in band i at assumed redshift z and spectral type T, and A is an arbitrary flux normalization and where the product extends over all nine bands. For each object, $\mathcal{L}(z,T)$ was maximized with respect to A and T to determine the "redshift likelihood function" $\mathcal{L}(z)$, which was maximized with respect to z to determine the maximum-likelihood photometric redshift.

3.4. Star and Galaxy Separation

We identified probable stars on the basis of visual inspection of the space-based images and the spectral energy distributions. Although in principle stars might be identified based solely on their spectrophotometric characteristics, in practice stars occur so infrequently in the HDF or HDF–S images that we decided not to incorporate stellar spectrophotometric templates into the photometric redshift analysis. A total of five probable stars were identified, the brightest of which is of magnitude $AB(16,000) \approx 17.2$ and the faintest of which is of magnitude $AB(16,000) \approx 21.1$. Table 2 lists properties of the probable stars.

4. RESULTS

4.1. Catalog of Photometry and Photometric Redshifts

The result of the analysis described in the previous section is a catalog of photometry and photometric redshifts of 335 objects in the HDF–S NICMOS field. The catalog is available on a World Wide Web site at `http://www.ess.sunysb.edu/astro/hdfs/index.html`. For each object, the catalog lists (1) the object identification, (2–3) the J2000 right ascension and declination, (4) the F160W magnitude $AB(16,000)$, (5–22) the relative energy flux density per unit frequency interval and uncertainty in the *U*, *B*, *V*, *R*, *I*, STIS, F110W, F160W, and F222M bands (with respect to the F160W band), (23) the best-fit photometric redshift, and (24) the best-fit spectral type. Here *AB* magnitude is related to energy flux density per unit frequency interval f_ν as

$$AB(\lambda) = -2.5 \log \frac{f_\nu(\lambda)}{1\ \mu\mathrm{Jy}} + 23.90. \tag{5}$$

The World Wide Web site also includes individual object pages that display the redshift likelihood functions, measured and modeled spectral energy distributions, and images of the objects.

4.2. Survey Area versus Depth Relation

The primary utility of the catalog of photometric redshifts is as a survey of faint galaxies detected in the NICMOS F160W image. Because the sensitivity of the F160W image varies significantly with position, the selection function of the survey is characterized by the survey area versus depth relation. We determined the survey area versus depth relation by assuming that the sensitivity image traces the shape (but not necessarily the normalization) of the sensitivity versus position relation of the F160W image. (The sensitivity image may not trace the normalization of the sensitivity versus position relation because of the non-zero off-diagonal elements of the covariance matrix.) First, we formed the sensitivity image by taking the square root of the variance image. Next, we scaled the sensitivity image so that it traced the faint-end envelope of the measured brightnesses of objects detected in the F160W image. Finally, we integrated the enclosed

area as a function of limiting depth to determine the survey area versus depth relation. Figure 7 shows the survey area versus depth relation, which indicates that the survey reaches a limiting depth of $AB(16,000) \approx 28.7$ and covers 1.01 arcmin^2 to $AB(16,000) = 27$ and 1.05 arcmin^2 to $AB(16,000) = 26.5$. Likewise, the survey reaches a limiting depth of $AB(22,200) \approx 24.8$ and covers 0.79 arcmin^2 to $AB(22,200) = 24$ and 1.09 arcmin^2 to $AB(22,200) = 23$. The survey area versus depth relation is crucial to any statistical analysis of the catalog.

5. EVALUATION OF THE PHOTOMETRIC REDSHIFT TECHNIQUE

5.1. Accuracy and Reliability of the Photometric Redshift Measurements

Spectroscopic redshift measurements of ≈ 120 faint galaxies in the HDF have been obtained using the Keck telescope (see, e.g., the list compiled by FLY99), and spectroscopic measurements of three galaxies in the HDF–S WFPC2 field have been obtained using the Anglo-Australian Telescope (Glazebrook et al. 2000, in preparation). Although more such measurements will undoubtedly be obtained (especially of faint galaxies in the HDF–S), the current measurements provide a means of assessing the accuracy and reliability of the photometric redshift measurements and of comparing results of the four- versus six-template photometric redshift measurements.

We compiled spectroscopic redshift measurements from published and unpublished sources, rejecting as unreliable spectroscopic measurements with uncertain or ambiguous interpretations. [A non-negligible fraction of the spectroscopic redshift measurements have been shown to be in error and so must be excluded from consideration; see, e.g., the discussions of Lanzetta, Fernández-Soto & Yahil (1998, hereafter LFY98) and FLY99.] Figure 7 shows the comparison of 104 photometric and reliable spectroscopic redshift measurements. Specifically, Figure 7(a) shows the comparison of the four-template photometric redshift measurements with the reliable spectroscopic redshift measurements, and Figure 7(b) shows the comparison of the six-template photometric redshift measurements with the reliable spectroscopic redshift measurements. Several results are evident on the basis of Figure 7:

1. Inclusion of the two new templates eliminates the tendency of our previous analyses to systematically underestimate the redshifts of galaxies of redshift $2 < z < 3$ (by a redshift offset of roughly 0.3), in agreement with results found previously by Benítez et al. (1998). The six-template photometric redshift measurements are essentially free of systematic bias at all redshifts $z < 6$ that have as yet been examined.

2. The RMS residual between the six-template photometric redshift measurements and the reliable spectroscopic redshift measurements is $\Delta z = 0.09$ at redshifts $z < 2$, $\Delta z = 0.29$ at redshifts $2 < z < 4$, and $\Delta z = 0.18$ at redshifts $z > 4$. The median absolute residual between the six-template photometric redshift measurements and the reliable spectroscopic redshift measurements is $\Delta z = 0.07$ at redshifts $z < 2$, $\Delta z = 0.22$ at redshifts $2 < z < 4$, and $\Delta z = 0.09$ at redshifts $z > 4$.

3. The six-template photometric redshift measurements are accurate to within an RMS relative uncertainty of $\Delta z/(1+z) \lesssim 7\%$ at all redshifts $z < 6$ that have as yet been examined.

We conclude that the photometric redshift technique is in general capable of determining reliable redshifts to within a relative uncertainty of $\Delta z/(1+z) \lesssim 7\%$.

5.2. Photometric Redshift Measurements of Stars

The photometric redshift measurements of the probable stars listed in Table 2 are $z = 0.07$, 0.30, 5.33, 5.63, and 5.72. Thus the spectral energy distributions of some stars resemble the spectral energy distributions of galaxies of redshift $z = 5 - 6$. We believe that all such stars were identified on the basis of visual inspection of the space-based images, but we cannot exclude the possibility that a small number of faint stars were misidentified as galaxies of redshift $z = 5 - 6$.

5.3. Effects of Photometric Error on the Photometric Redshift Measurements

Comparison of the photometric and spectroscopic redshift measurements yields a measure of the uncertainties of the photometric redshift technique, which in principle can include contributions from both photometric error and cosmic variance with respect to the spectral templates. At bright magnitudes, the effects of photometric error are expected to be negligible, while at faint magnitudes the effects of photometric error are expected to dominate.

We assessed the effects of photometric error on the photometric redshift measurements by performing a series of simulations similar to those described previously by LFY98. First, we determined the expected energy fluxes through the various filters of an Irr galaxy spectrophotometric template, given an assumed galaxy magnitude $AB(16,000)$ [selected over the range $21 < AB(16,000) < 29$] and redshift z (selected over the range $0 < z < 11$). Next, we added random noise to the expected energy fluxes according to the actual noise characteristics of the images. Next, we determined photometric redshift measurements of the simulated objects using the sequence of six spectrophotometric templates. Finally, we repeated these steps 1000 times as functions of $AB(16,000)$ and z to determine the distribution of redshift residuals between the input and output models. Figure 7 shows the distributions of redshift residuals as functions of $AB(16,000)$ and z. Several results are evident on the basis of Figure 7:

1. At $AB(16000) < 25$, photometric errors have a negligible effect on the photometric redshift measurements. At these relatively bright magnitudes, the RMS dispersion of the residuals is $\Delta z \lesssim 0.02$.

2. At $AB(16000) = 25 - 26$, photometric errors have only a modest effect on the photometric redshift measurements at redshifts $z \lesssim 7$, where the RMS dispersion of the residuals is $\Delta z \lesssim 0.25$, but have a somewhat more significant effect on the photometric redshift measurements at

$z \gtrsim 7$, where a secondary peak in the residual distribution occurs at large negative residual, i.e. at $\Delta z \approx -6$. The secondary peak is caused by ambiguity between high-redshift late-type galaxies and low-redshift early-type galaxies.

3. At $AB(16000) = 27-28$, photometric errors have a modest effect on the photometric redshift measurements at all redshifts, with a prominent secondary peak in the residual distribution at all redshifts $z \gtrsim 3$. The sense of the secondary peak is such that it is more likely for high-redshift objects to be assigned low redshifts than for low-redshift objects to be assigned high redshifts.

4. At $AB(16000) > 28$, photometric errors have a significant effect on the photometric redshift measurements at all redshifts.

We conclude that the effects of photometric error on the photometric redshift measurements must be taken into consideration at magnitudes fainter than $AB(16,000) \approx 25$.

6. DISCUSSION

Here we briefly discuss results of the catalog of photometric redshifts, concentrating on results related to the highest-redshift galaxies identified by the analysis. Scientific analysis of the catalog will be presented in forthcoming papers.

6.1. Redshift Distribution of Galaxies in the HDF–S NICMOS Field

The catalog of photometric redshifts identifies 330 galaxies, of photometric redshift measurement ranging from $z \approx 0$ through $z > 10$. Figure 7 shows the redshift distribution of the galaxies in the HDF–S NICMOS field. The distribution is characterized by a median redshift of $z_{\rm med} = 1.38$ and by a tail that stretches to redshifts beyond $z = 10$. The redshift distribution of Figure 7 does not, of course, apply for any magnitude-limited sample, because the sensitivity of the F160W image varies significantly with position.

6.2. Galaxies of Redshift $z > 5$

One difference between the current analysis of the HDF–S NICMOS field and our previous analyses of the HDF is that the current analysis is in principle sensitive to galaxies of redshift larger than was the previous analyses. In this section, we discuss the galaxies of photometric redshift measurement $z > 5$.

The catalog of photometric redshifts identifies 21 galaxies (or 6% of the total) of redshift $z > 5$. Table 3 lists the positions, magnitudes $AB(16,000)$, photometric redshift measurements z, and best-fit spectral types of these galaxies, and Figure 7 shows the observed and modeled

spectral energy distributions and redshift likelihood functions of these galaxies. Table 4 lists surface densities of galaxies of redshift $z > 5$ derived from the catalog of photometric redshifts accounting for the variation of the survey area versus depth relation as a function of limiting magnitude $AB(16,000)$. Uncertainties listed in Table 4 are derived by a bootstrap resampling technique, which explicitly accounts for sampling error, photometric error, and cosmic variance with respect to the spectrophotometric templates. First, we resampled the original catalog, allowing the possibility of duplication. Next, we added random noise to the flux measurements (according to the actual noise properties of the images) and redetermined the photometric redshift measurements. Next, we added random noise to the photometric redshift measurements (according to the actual noise properties of the photometric redshift technique, as described in § 5.1). Next, we measureed galaxy surface densities from the resampled and perturbed photometric redshift catalog. Finally, we repeated these steps a thousand times and determine the 1 σ deviations of the surface density measurements. We conclude that galaxies of redshift $z > 5$ are a non-negligible fraction of the galaxy population at magnitudes $AB(16,000) \gtrsim 27$.

6.3. Galaxies of Redshift $z > 10$

The catalog of photometric redshifts identifies 8 galaxies (or 2% of the total) of redshift $z > 10$ including 3 galaxies detected on the basis of the F222M image. Table 5 lists surface densities of galaxies of redshift $z > 10$ derived from the catalog of photometric redshifts accounting for the variation of the survey area versus depth relation as a function of limiting magnitudes $AB(16,000)$ and $AB(22,200)$. We are struck that the surface density of galaxies of redshift $z > 10$ at $AB(22,200) = 24$ is comparable to the surface density of galaxies of redshift $z > 10$ at $AB(16,000) = 28$.

6.4. Early-Type Galaxies of Redshift $z > 1$

Another difference between the current analysis of the HDF–S NICMOS field and our previous analyses of the HDF is that the current analysis is in principle sensitive to early-type galaxies of redshift larger than was the previous analyses. In this section, we discuss the early-type galaxies of photometric redshift measurement $z > 1$.

The catalog of photometric redshifts identifies 11 galaxies (or 3% of the total) of best-fit spectral type E/S0, of which 5 galaxies (or 1% of the total) are of redshift $z > 1$. Table 6 lists the positions, magnitudes $AB(16,000)$, photometric redshift measurements z, and Figure 7 shows the observed and modeled spectral energy distributions and redshift likelihood functions of these galaxies. (It should be noted, however, that the likelihood that SB–NI–0471–0941 is an early–type galaxy of redshift $z = 5.10$ is statistically indistinguishable from the likelihood that this object is a later–type galaxy of redshift $z \gtrsim 10$. A similar result also applies for SB–NI–0844–0698.)

Table 7 lists surface densities of early-type galaxies of redshift $z > 1$ derived from the catalog of photometric redshifts and the survey area versus depth relation as a function of limiting magnitude $AB(16,000)$. (Uncertainties listed in Table 7 are derived as in Table 4.) We conclude that early-type galaxies of redshift $z > 1$ are a non-negligible fraction of the galaxy population at magnitudes $AB(16,000) \gtrsim 25$.

6.5. Comparison with Other Photometric Redshift Measurements

Table 8 compares photometric redshift measurements of six galaxies in common between the current analysis and the previous analysis of Benítez et al. (1999). Four of the six pairs of measurements are concordant and two of the six pairs of measurements are discordant to within the cosmic dispersion $\Delta z \approx 0.1$ of the photometric redshift measurement technique as described in § 5.1.

Benítez et al. (1999) used similar photometric redshift techniques and template spectra, so the discrepancies most likely arise from differences in photometry. Comparison of photometry in all bands indicates that, while our flux measurements are consistent with the flux measurements of Benítez et al. (1999) in the optical and the F160W bands, our flux measurements are systematically lower in the F110W band and systematically higher in the F222M band. These differences arise because we use a spatial profile fitting technique, which takes into account differences in the PSF from band to band, whereas Benítez et al. (1999) use a fixed aperture technique (where the apertures are determined from a combined F110W and F160W image), which implicitly assumes identical PSFs in all bands. There are indeed differences in the PSFs for the three NICMOS images. The PSF of the F222M image is slightly broader than the PSF of the F160W image, and the PSF of the F110W image is slightly sharper than the PSF of the F160W image. We therefore suspect that Benítez et al. (1999) may have overestimated fluxes in the F110W image (because the apertures were too large) and underestimated fluxes in the F222M image (because the apertures were too small).

7. SUMMARY AND CONCLUSIONS

Here we present a catalog of photometry and photometric redshifts of 335 faint objects in the HDF–S NICMOS field. The analysis is based on (1) infrared images obtained with HST using NICMOS with the F110W, F160W, and F222M filters, (2) an optical image obtained with HST using STIS with no filter, and (3) optical images obtained with the ESO VLT with U, B, V, R, and I filters. The primary utility of the catalog of photometric redshifts is as a survey of faint galaxies detected in the NICMOS F160W and F222M images. The sensitivity of the survey varies significantly with position, reaching a limiting depth of $AB(16,000) \approx 28.7$ and covering 1.01 arcmin^2 to $AB(16,000) = 27$ and 1.05 arcmin^2 to $AB(16,000) = 26.5$. Likewise, the survey reaches

a limiting depth of $AB(22,200) \approx 24.8$ and covering 0.79 arcmin^2 to $AB(22,200) = 24$ and 1.09 arcmin^2 to $AB(22,200) = 23$. The catalog of photometric redshifts identifies 21 galaxies (or 6% of the total) of redshift $z > 5$, 8 galaxies (or 2% of the total) of redshift $z > 10$, and 11 galaxies (or 3% of the total) of best-fit spectral type E/S0, of which 5 galaxies (or 1% of the total) are of redshift $z > 1$.

The authors thank Bob Williams and the entire STScI HDF–S team for providing access to the HDF–S observations, the entire ESO VLT team for making observations of the HDF–S publicly available, and an anonymous referee for helpful comments. HWC, KML, SMP, and NY were supported by NASA grant NAGW–4422 and NSF grant AST–9624216. AFS was supported by a grant from the Australian Research Council. RCP was supported by NASA grant NAG–53944. AY was supported by NASA grant AR–07551.01–96A.

REFERENCES

Benítez, N. 1999, ApJ, submitted (astro-ph/9811189)

Benítez, N., Broadhurst, T., Bouwens, R., Silk, J., & Rosati, P. 1999, ApJ, 515, L65

Bertin, E., & Arnouts, S. 1996, A&AS, 117, 393

Fernández-Soto, A., Lanzetta, K. M., & Yahil, A. 1999, ApJ, 513, 34

Fontana, A., D'Odorico, S., Fosbury, R., Giallongo, E., Hook, R., Poli, F., Renzini, A., Rosati, P., & Viezzer, R. 1999, A&A, 343, L19

Glazebrook, K. et al. 2000, in preparation

Kinney, A. L., Calzetti, D., Bohlin, R. C., McQuade, K., Storchi-Bergmann, & T., Schmitt, H. R. 1996, ApJ, 467, 38

Lanzetta, K. M., Yahil, A., & Fernández-Soto, A. 1996, Nature, 381, 759

Lanzetta, K. M., Fernández-Soto, A., & Yahil, A. 1998, in The Hubble Deep Field, Proceedings of the Space Telescope Science Institute 1997 May Symposium, ed. M. Livio, S. M. Fall, & P. Madau (Cambridge: Cambridge University Press), p. 143

Madau, P. 1995, ApJ, 441, 18

Puetter, C. R., & Yahil, A. 1999 in ASP Conf. Ser., Vol. 172, Astronomical Data Analysis Software and Systems VIII, eds. D. M. Mehringer, R. L. Plante, & D. A. Roberts (San Francisco: ASP), p. 307

Webb, J. K. 1996, unpublished

This preprint was prepared with the AAS LaTeX macros v5.0.

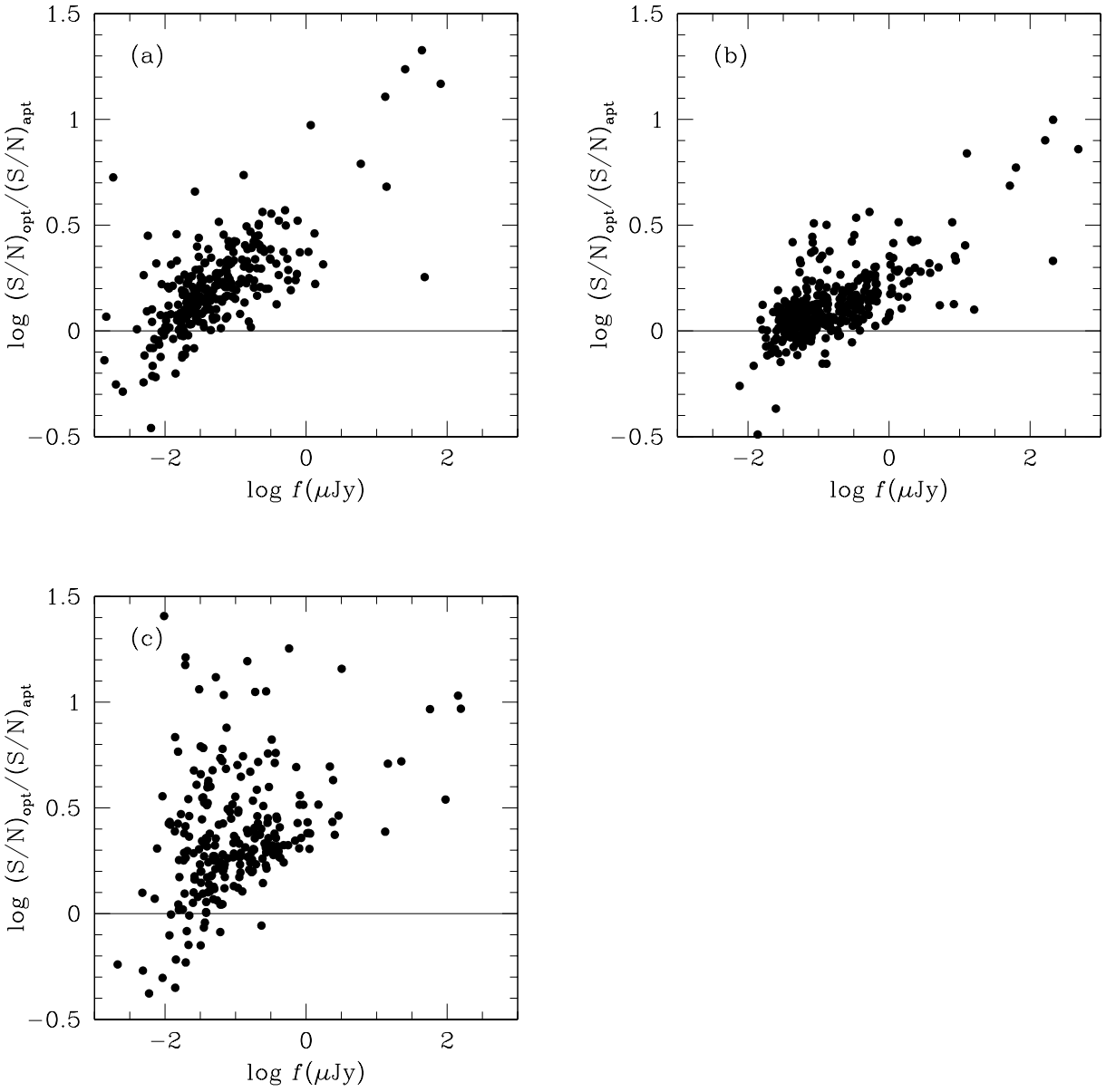

Fig. 1.— Comparison of signal-to-noise ratios obtained by quasi-optimal photometry method and by direct integration within isophotal apertures versus logarithm of energy flux obtained by quasi-optimal photometry method for (a) STIS image, (b) NICMOS F160W image, and (c) VLT I-band image. The signal-to-noise ratios obtained by the quasi-optimal photometry method are in general larger than the signal-to-noise ratios obtained by direct integration within isophotal apertures.

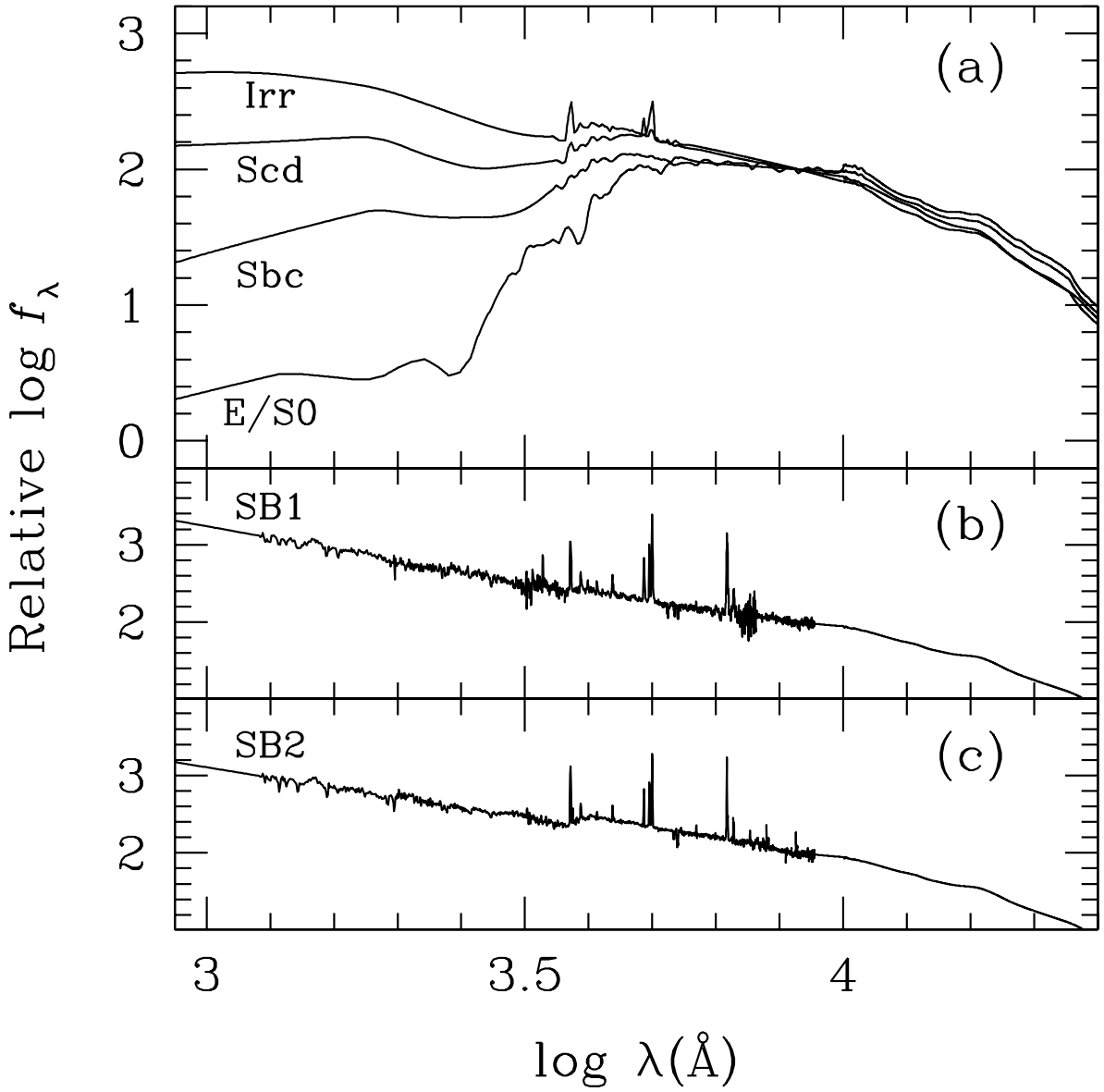

Fig. 2.— Spectral energy distributions of (a) E/S0, Sbc, Scd, and Irr galaxies, (b) SB1 galaxy, and (c) SB2 galaxy.

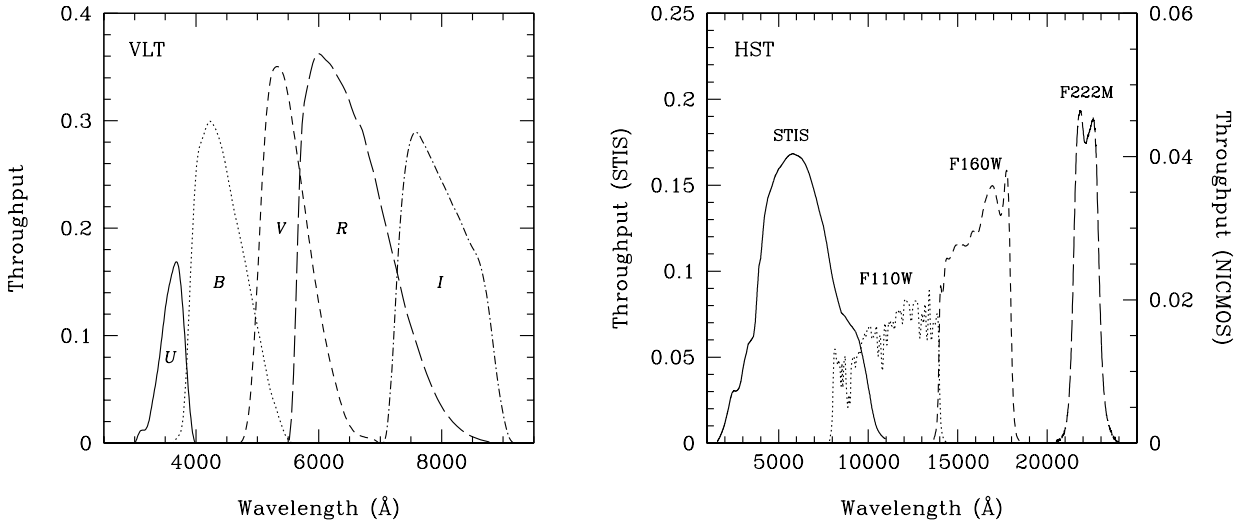

Fig. 3.— System throughput functions of (a) the VLT with the Test Camera and the U, B, V, R, and I filters and (b) HST with STIS and with NICMOS and the F110W, F160W, and F222M filters.

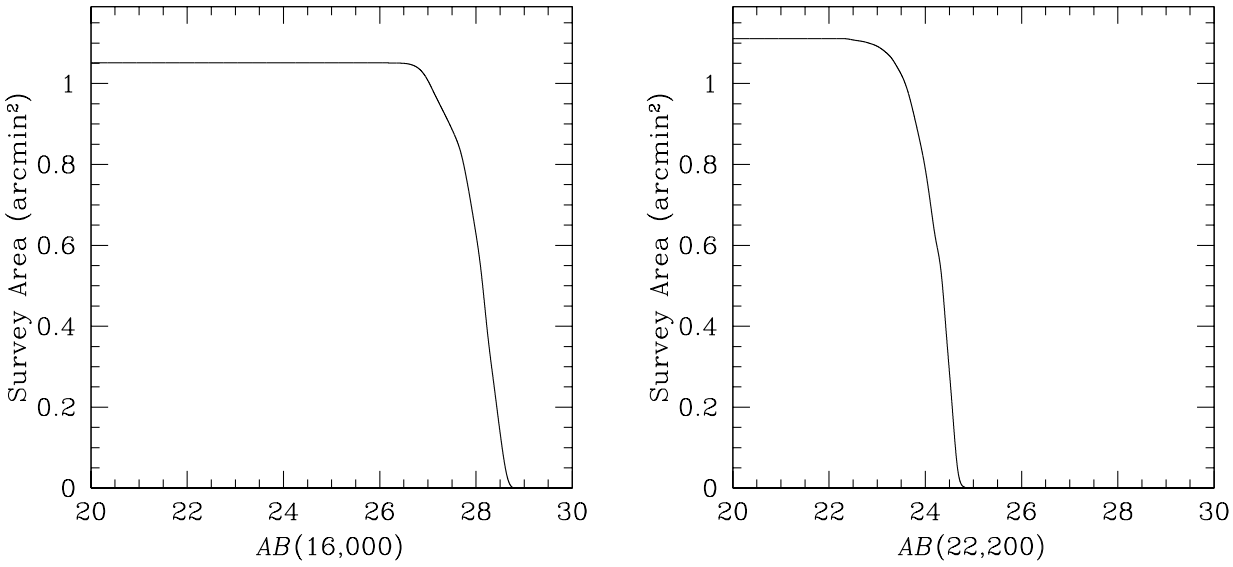

Fig. 4.— Survey area versus depth relation on the basis of (a) NICMOS F160W image and (b) NICMOS F222M image.

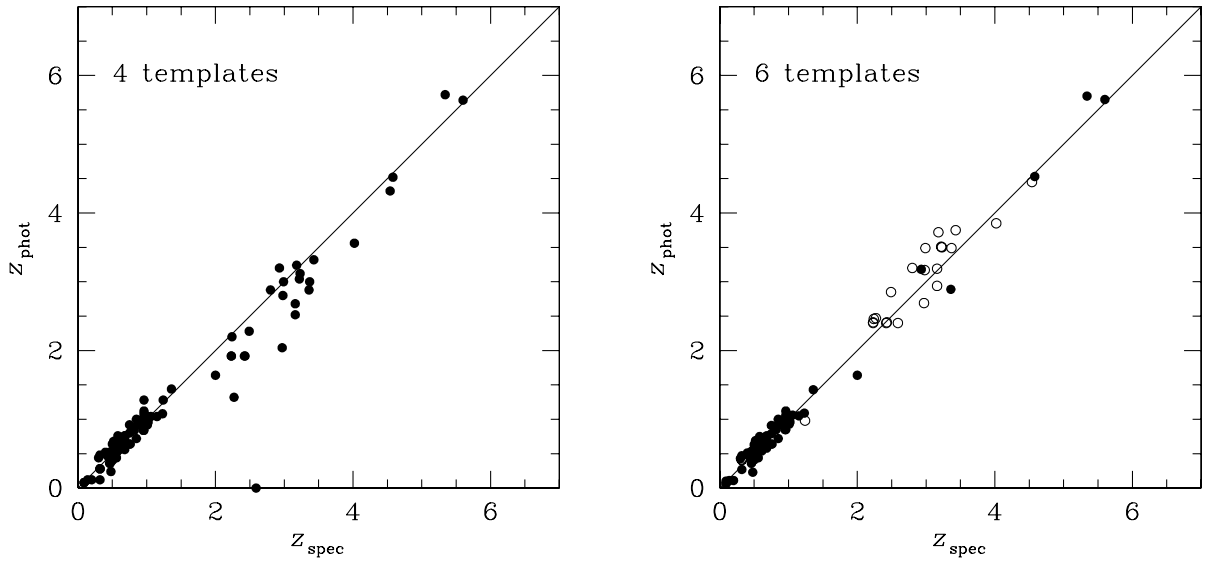

Fig. 5.— Comparison of 104 photometric and reliable spectroscopic redshift measurements for (a) four-template photometric redshift measurements and (b) six-template photometric redshift measurements. Filled circles represent E/S0, Sbc, Scd, and Irr best-fit spectral types, and open circles represent SB1 and SB2 best-fit spectral types.

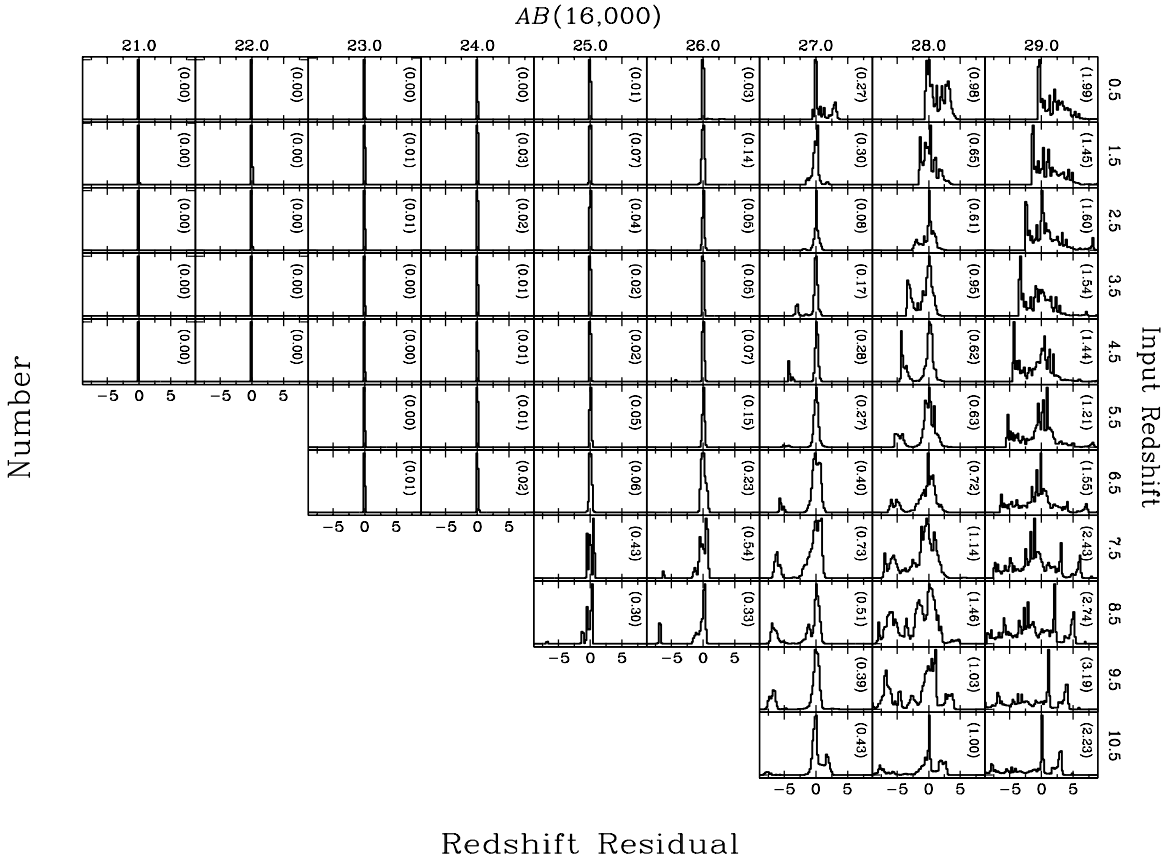

Fig. 6.— Distribution of redshift residuals as functions of galaxy magnitude $AB(16,000)$ and redshift z. The number in parentheses gives the median absolute deviation of the output redshift from the input redshift for each panel.

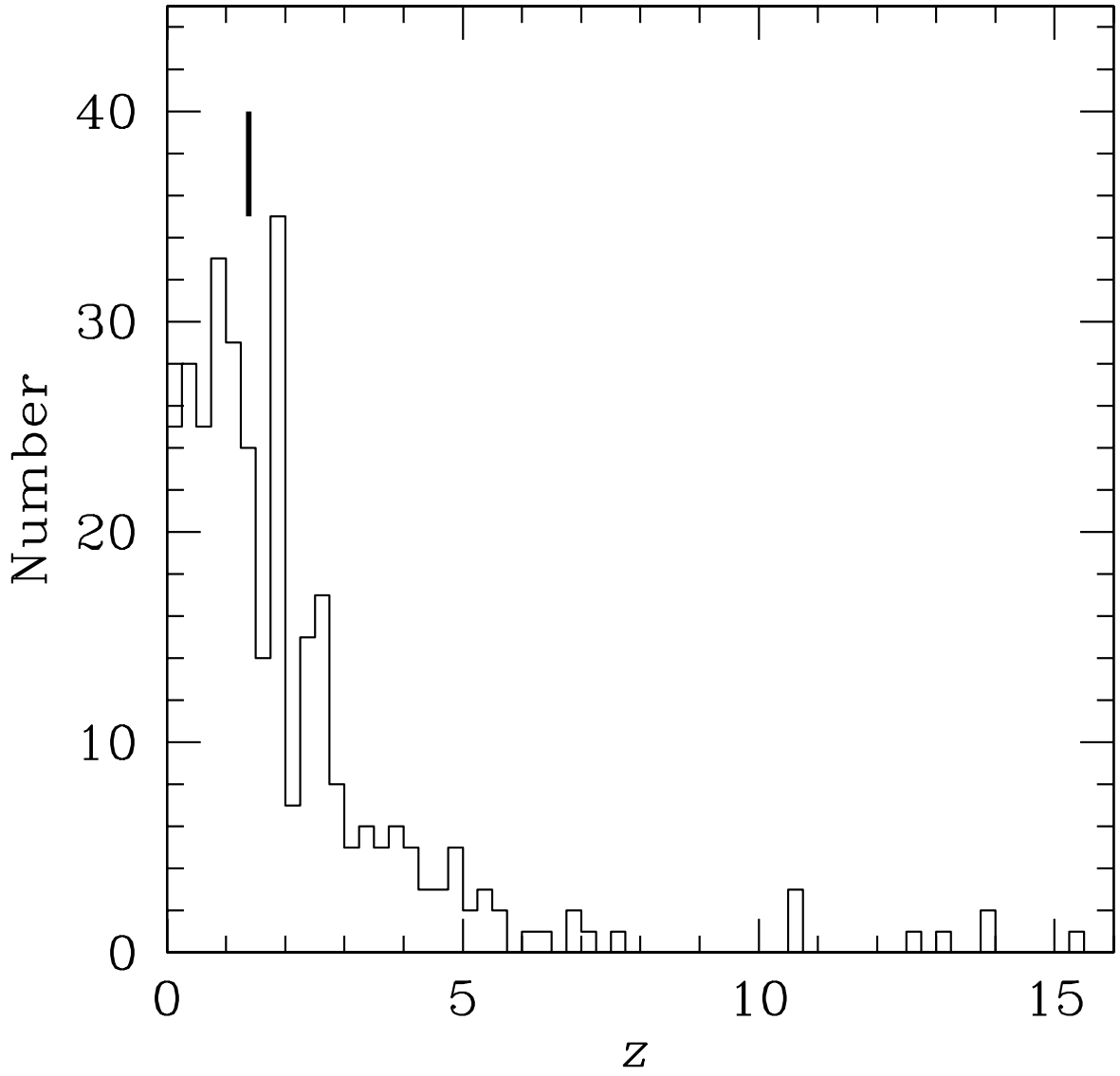

Fig. 7.— Redshift distribution of galaxies identified in the HDF–S NICMOS field. Line segment indicates median redshift.

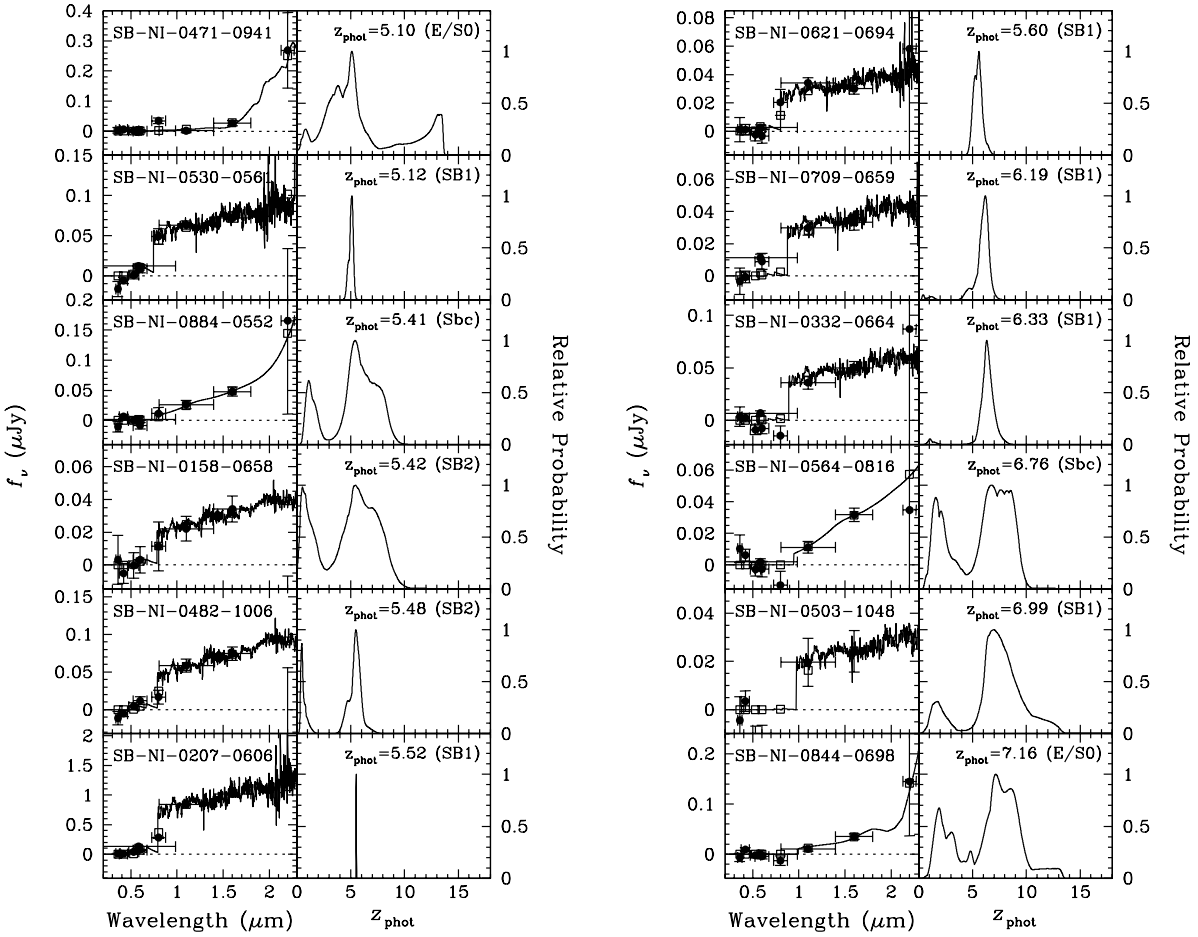

Fig. 8.— Observed and modeled spectral energy distributions (left panels) and redshift likelihood functions (right panels) of galaxies of photometric redshift measurement $z > 5$. Filled circles are measured fluxes and open squares are best-fit model fluxes. Vertical error bars indicate 1σ uncertainties and horizontal error bars indicate filter FWHM. Photometric redshift measurement and best-fit spectral type of each galaxy are indicated.

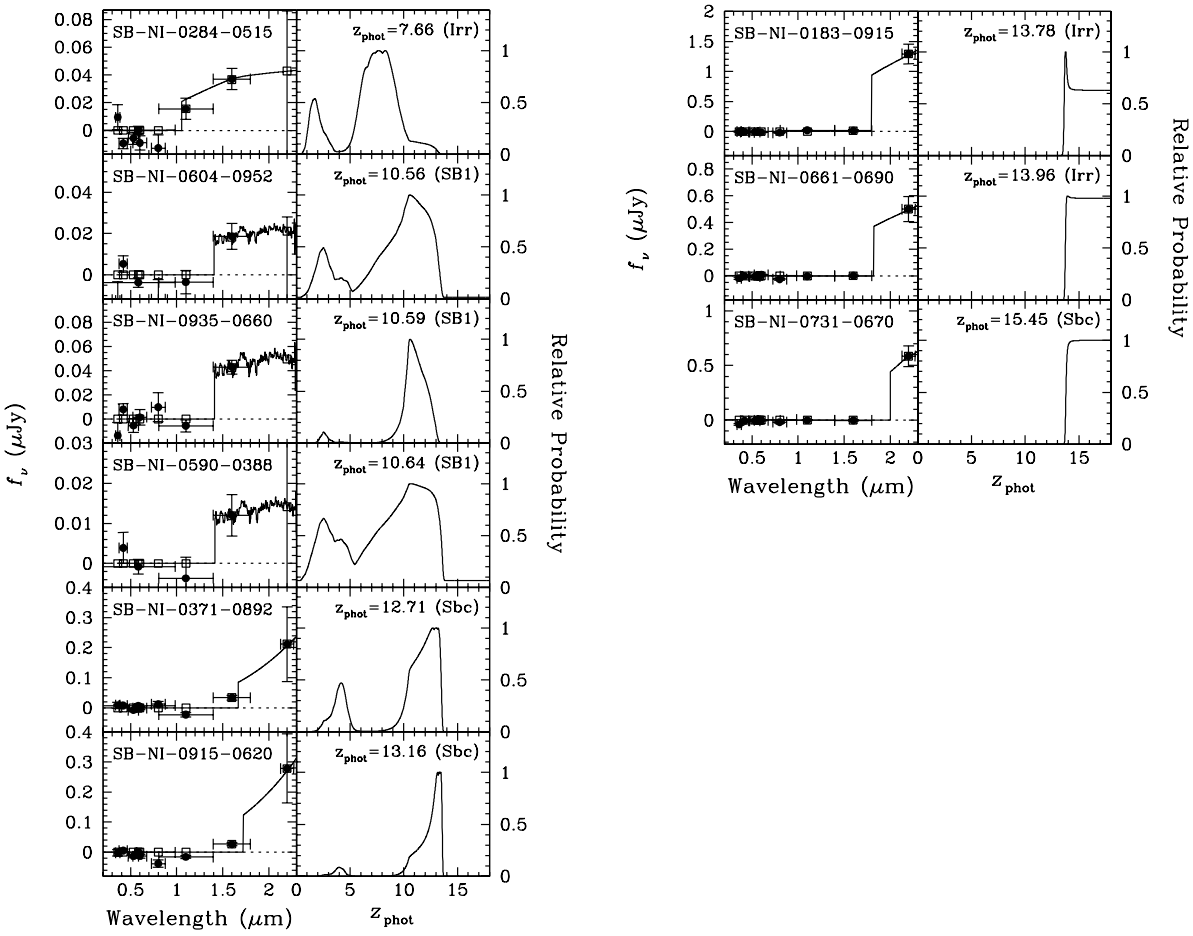

Fig. 8.— — *Continued.*

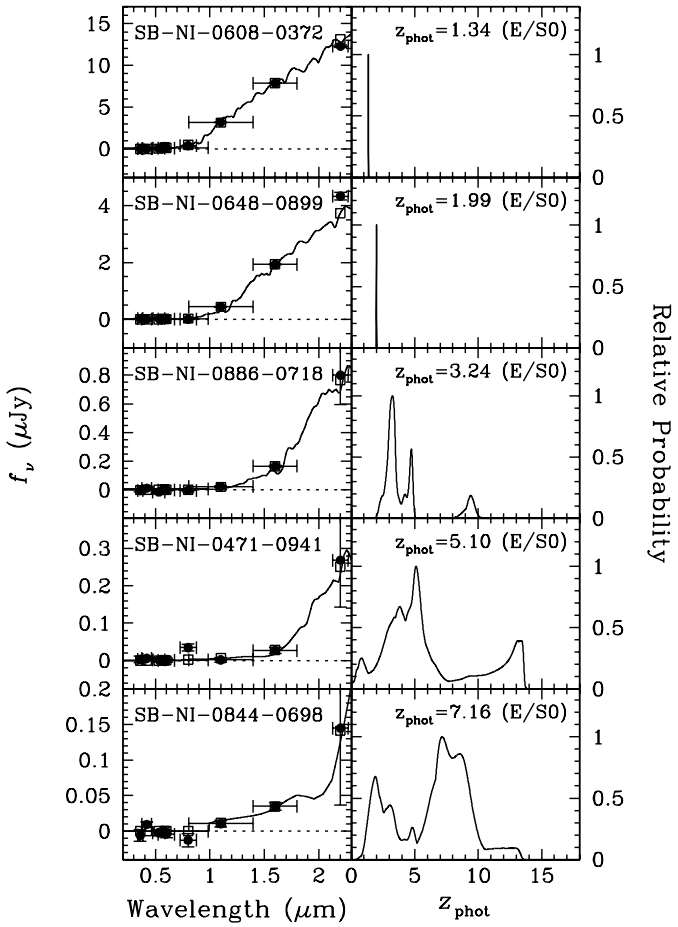

Fig. 9.— Observed and modeled spectral energy distributions (left panels) and redshift likelihood functions (right panels) of early-type galaxies of photometric redshift measurement $z > 1$. Filled circles are measured fluxes and open squares are best-fit model fluxes. Vertical error bars indicate 1σ uncertainties and horizontal error bars indicate filter FWHM. Photometric redshift measurement and best-fit spectral type of each galaxy are indicated.

Table 1. Details of the Observations

Instrument	Filter	λ (Å)	$\Delta\lambda$ (Å)	Exposure Times (s)
ESO VLT (UT1)	VLT-TC U	3600	500	32,400
	VLT-TC B	4200	900	10,800
	VLT-TC V	5300	1100	10,800
	SUSI2 #825 R	6000	1500	10,800
	VLT-TC I	8000	1500	14,400
HST STIS 50CCD	···	5835	8000	25,900
HST NICMOS Camera 3	F110W	10,985	5915	108,539
	F160W	15,940	4030	128,441
	F222M	22,160	1432	103,163

Table 2. Probable Stars

Object	α	δ	$AB(16,000)$
SB–NI–0157–0534	22:32:55.69	−60:38:57.59	21.14
SB–NI–0277–0904	22:32:54.47	−60:38:29.88	17.19
SB–NI–0278–0599	22:32:54.46	−60:38:52.75	18.37
SB–NI–0446–0431	22:32:52.75	−60:39:05.35	18.09
SB–NI–0774–0562	22:32:49.40	−60:38:55.53	19.40

Table 3. Galaxies of Redshift $z > 5$

Object	α	δ	$AB(16,000)$	$z_{\rm phot}$	Type
SB–NI–0471–0941	22:32:52.49	−60:38:27.08	27.83	5.10	E/S0
SB–NI–0530–0561	22:32:51.89	−60:38:55.57	26.76	5.12	SB1
SB–NI–0884–0552	22:32:48.28	−60:38:56.24	27.20	5.41	Sbc
SB–NI–0158–0658	22:32:55.68	−60:38:48.28	27.56	5.42	SB2
SB–NI–0482–1006	22:32:52.38	−60:38:22.18	26.72	5.48	SB2
SB–NI–0207–0606	22:32:55.18	−60:38:52.17	23.88	5.52	SB1
SB–NI–0621–0694	22:32:50.96	−60:38:45.63	27.71	5.60	SB1
SB–NI–0709–0659	22:32:50.07	−60:38:48.25	27.59	6.19	SB1
SB–NI–0332–0664	22:32:53.91	−60:38:47.82	27.15	6.33	SB1
SB–NI–0564–0816	22:32:51.54	−60:38:36.42	27.65	6.76	Sbc
SB–NI–0503–1048	22:32:52.16	−60:38:19.05	27.94	6.99	SB1
SB–NI–0844–0698	22:32:48.69	−60:38:45.28	27.54	7.16	E/S0
SB–NI–0284–0515	22:32:54.40	−60:38:59.01	27.48	7.66	Irr
SB–NI–0604–0952	22:32:51.13	−60:38:26.23	28.23	10.56	SB1
SB–NI–0935–0660	22:32:47.75	−60:38:48.14	27.32	10.59	SB1
SB–NI–0590–0388	22:32:51.28	−60:39:08.53	28.70	10.64	SB1
SB–NI–0371–0892	22:32:53.51	−60:38:30.77	27.58	12.71	Sbc
SB–NI–0915–0620	22:32:47.97	−60:38:51.13	27.84	13.16	Sbc
SB–NI–0183–0915	22:32:55.43	−60:38:29.03	$23.62^{\dagger}$	13.78	Irr
SB–NI–0661–0690	22:32:50.55	−60:38:45.90	$24.65^{\dagger}$	13.97	Irr
SB–NI–0731–0670	22:32:49.84	−60:38:47.40	$24.48^{\dagger}$	15.45	Sbc

$^{\dagger}AB(22,200)$

Table 4. Surface Densities of Galaxies of Redshift $z > 5$

$AB(16,000)$	N (arcmin^{-2})	$\sigma(N)$ (arcmin^{-2})
26.0	0.95	0.95
27.0	2.87	1.90
28.0	18.32	3.81

Table 5. Surface Densities of Galaxies of Redshift $z > 10$

Magnitude	N (arcmin^{-2})	$\sigma(N)$ (arcmin^{-2})
$AB(16,000) = 28.0$	3.58	$^{+1.90}_{-0.95}$
$AB(22,200) = 24.0$	1.01	$^{+0.90}_{-0.90}$

Table 6. Early-Type Galaxies of Redshift $z > 1$

Object	α	δ	$AB(16,000)$	$z_{\rm phot}$
SB–NI–0608–0372	22:32:51.09	−60:39:09.75	21.66	1.35
SB–NI–0648–0899	22:32:50.69	−60:38:30.26	23.19	1.99
SB–NI–0886–0718	22:32:48.26	−60:38:43.78	25.85	3.24
SB–NI–0471–0941	22:32:52.49	−60:38:27.08	27.83	5.10
SB–NI–0844–0698	22:32:48.69	−60:38:45.28	27.54	7.16

Table 7. Surface densities of Early-Type Galaxies of Redshift $z > 1$

$AB(16,000)$	N (arcmin^{-2})	$\sigma(N)$ (arcmin^{-2})
25.0	1.90	$^{+1.90}_{-0.95}$
26.0	2.85	$^{+1.90}_{-0.95}$
27.0	2.85	$^{+1.90}_{-0.95}$
28.0	5.33	$^{+1.90}_{-2.85}$

Table 8. Comparison of Photometric Redshift Measurements

Current Analysis				Analysis of Benítez et al. (1999)			
Object	$AB(16,000)$	$z_{\rm phot}$	Type	Object	$AB(16,000)$	$z_{\rm phot}$	Type
SB–NI–0181–0870 ...	21.20	0.98	E/S0	NIC3–ET1	21.24	1.41	E
SB–NI–0440–0353 ...	24.34	2.23	Sbc	NIC3–ET2	24.50	1.55	E
SB–NI–0608–0372 ...	21.66	1.35	E/S0	NIC3–ET3	21.79	1.66	E
SB–NI–0648–0899 ...	23.19	1.99	E/S0	NIC3–ET4	23.18	1.94	E
SB–NI–0596–1002 ...	23.45	1.93	Sbc	NIC3–SP1	23.53	2.1	Sab
SB–NI–0837–1023 ...	22.10	1.39	Scd	NIC3–SP2	22.33	1.2	Sbc